An evaluation of EO-1 Hyperion data in mapping surficial geology near Loiyangalani, Northern Kenya

Joshua Zoellmer
Senior Integrative Exercise
March 12, 2014

Submitted in partial fulfillment of the requirements for a Bachelor of Arts degree from Carleton College, Northfield, Minnesota

Table of Contents

An evaluation of EO-1 Hyperion data in mapping surficial geology near Loiyangalani, Northern Kenya

Joshua Zoellmer
Carleton College
Senior Integrative Exercise
March 12, 2014

Advisors:
Tsegaye Nega, Carleton College, Northfield, MN
Bereket Haileab, Carleton College, Northfield, MN

ABSTRACT

Air- and spaceborne hyper- and multispectral sensors have played an important role in efforts to map regional-scale areas for the purposes of geologic mapping and remote mineral exploration. One such instrument is the EO-1 Hyperion spaceborne hyperspectral spectrometer. The purpose of this paper is to examine the ability of Hyperion to map the surficial geology of a non-hydrothermally altered area at the southeastern tip of Lake Turkana, Kenya. The Spectral Angle Mapper (SAM) method of showing the distribution was compared to the Mixtured Tuned Matched Filtering (MTMF) method in order to analyze the user-defined endmembers of image spectra. The results showed the presence of goethite, hematite, kaolinite/smectite, desert varnish and lamprophyre. With the exception of lamprophyre, these materials represent the most common weathering products of basalt and attest to Hyperion's ability to produce realistic results. These results coupled with the established presence of alkaline rocks in rift settings give promise to the existence of previously undiscovered or misclassified lamprophyre. Additional analysis with SAM images failed to match pixel spectra to that of basalt or gneiss, but confirmed the presence of hematite. Further testing through ground truthing is required to validate these results.

Keywords: EO-1 Hyperion; Hyperspectral; imaging spectroscopy; Lake Turkana; Loiyangalani

INTRODUCTION

The study of geology is often concerned with large regions of study. Because many geologic processes take place on the macro scale, it is very important for studies to investigate and map regions on the order of kilometers. However, the need for detailed data about a large area poses a unique problem for scientists. Creating a map at this scale often involves strategically collecting samples in various locations dispersed throughout the study area then interpreting the results and inferring what may be in the areas that were not visited. There is an obvious sacrifice of accuracy in this method. This is especially true in identifying and locating rock formations, and detailed characteristics such as mineral composition rocks are excluded from such studies. While Curtiss et al. (2012) demonstrated the ability of field-portable reflectance spectrometers to accurately identify minerals, this approach is time and labor intensive and not practical for the mapping of many hundreds of square kilometers. Recently, geologists have turned to air- and spaceborne imaging spectrometers as an efficient and cost effective way to gain insight about the mineralogy and lithology at a regional scale.

This paper investigates a region to the south of Lake Turkana that has not yet been analyzed by EO-1 Hyperion hyperspectral data. Furthermore, this area lacks any hydrothermal alteration. Because hyperspectral remote spectroscopy has historically been used to locate minerals associated with hydrothermally altered zones, there exists a deficit of literature about Hyperion's ability to classify non-hydrothermally altered minerals.

Through the use of the ENVI 5.0 image analysis software, this study analyzes the ability of Hyperion to identify the surface rocks and minerals near Loiyangalani, Kenya.

Distribution maps created with both the Spectral Angle Mapper (SAM) and Mixture Tuned Matched Filtering (MTMF) methods are presented as visual tools for evaluating Hyperion's ability to provide plausible endmember results. Finally, SAM mapping was applied to pixel spectra in attempts of finding positive matches for expected rocks.

BACKGROUND

Hyperspectral Sensors

The advantages of remote spectroscopy for use in geology have been realized for decades. Since NASA introduced the first scanning imaging spectrometer in the early 1970s, governments and private companies have developed instruments for remote spectroscopy (van der Meer et al., 2012). Of the most notable early airborne spectrometers is NASA's Airborne Visible/Infrared Imaging Spectrometer (AVIRIS). Operational since 1987, AVIRIS is still in use and represents the current standard for remote spectroscopy (van der Meer et al., 2012). Also of note are the Airborne Imaging Spectrometer for Applications (AISA) family of instruments, and the HYperspectral MAPper (HYMAP) airborne sensors created by private companies (van der Meer et al., 2012) .

In 1997 the LEWIS Hyperspectral Imager (HSI) ushered in a new era of imaging spectroscopy when it became the first imaging spectrometer on a satellite platform. The instrument failed, but set the stage for the Hyperion hyperspectral spectrometer (van der Meer et al., 2012). Based on the HSI concept, Hyperion became the first successful space-based instrument of its kind when launched in November of 2000 (Kruse, 2002; van der Meer et al., 2012).

EO-1 Hyperion

Table 1 offers a comparison of two hyperspectral spectrometers, NASA's Hyperion and Airborne Visible/Infrared Imaging Spectrometer (AVIRIS)

Table 1. Comparison of NASA's Hyperion and AVIRIS hyperspectral imaging spectrometers. Data from (Kruse, 2002).

	Hyperion	**AVIRIS**
Number of bands	242	224
Spectral resolution	10 nm	10 nm
Spectral range	400-2500 nm	400-2500 nm
Signal-to-Noise Ratio (SNR)	50:1	500:1
Spatial resolution	30 m	20 m
Width of collection area	7.5 km	10.5 km
Altitude of collection	705 km	20 km
Collection vehicle	EO-1 satellite	ER-2 aircraft

There are two major differences between the two systems, and they are intimately connected. Because of the altitudinal difference from which the two systems are collected, the signal-to-noise ratio of AVIRIS is ten times better than that of Hyperion. This is due to the fact that Hyperion's sensors are mounted on a satellite, while AVIRIS is mounted on a plane that flies at an altitude around 20 km and thus experiences less atmospheric scattering. This advantage allows AVIRIS to collect spectra that are more accurate than Hyperion's. In some cases, Hyperion has been known to misclassify minerals with similar compositions like dolomite and calcite and in other cases has been unable to extract spectra because of the high signal-to-noise ratio (Kruse, 2002). Despite Hyperion's shortcomings, a study by Kruse (2002) comparing Hyperion and AVIRIS data showed that when used for basic mineral mapping the two spectrometers provide similar results and that the difference in pixel size (spatial resolution) was inconsequential.

Hyperion's hyperspectral capabilities make it an invaluable tool in a variety of situations across all scientific fields of study. For example, Guerschman et al. (2009) and Pignatti et al. (2009) effectively demonstrated Hyperion's ability to classify vegetation in order to identify vegetation diversity and create land cover classes. However, Hyperion, like all hyperspectral spectrometers, is used most intensively in geology, driven primarily by mineral exploration (van der Meer et al., 2012). The use of Hyperion images in creating accurate maps of minerals associated with mineral extraction is well documented (Onuma et al., 2005; Mauger et al., 2007; Khan et al., 2011; Pour et al., 2013). Because geochemical processes cause the formation of economically viable mineral deposits in hydrothermally altered areas, alteration zones and associated minerals have been extensively mapped (Crosta et al., 2008; Nikolakopoulos et al., 2008; Diaz-Castellon et al., 2012; Ball et al., 2013). To a lesser extent, Hyperion images have been used to classify soil content (Lu et al., 2013), map contamination of tailings from abandoned ore mines (Riaza et al., 2012), and locate hydrocarbon microseepages (Jacobson et al., 2006; Petrovic et al., 2008).

Electromagnetic Spectrum

The information that is recorded by the spectrometer comes in the form of electromagnetic radiation that has been reflected, emitted, or both reflected and emitted from a source. Of these three forms, reflected energy is the most important for remote sensing (Chuvieco, 2009). Electromagnetic radiation is described using both the wave theory and quantum theory, meaning the energy is both wave-like and particle-like. The

wave theory states that wavelength and frequency are inversely related and is expressed with the equation:

$$c = \lambda \upsilon$$

where c is the speed of light in a vacuum, λ is wavelength and υ is frequency. On the other hand, quantum theory states that energy is both proportional to the frequency of the incident radiation and quantized, as seen in the equation:

$$E = h\upsilon = \frac{hc}{\lambda}$$

where E is the energy of a photon, h is Planck's constant, υ is frequency, c is the speed of light in a vacuum, and λ is wavelength.

Though it encompasses a continuum of wavelengths, the electromagnetic spectrum is divided into discrete regions. Of greatest importance to remote sensing are the visible and infrared regions. The visible region is a very narrow slice of the spectrum, ranging from approximately 400 to 700 nm in wavelength, and is so named because it is the range of wavelengths that are detectable by the human eye. The visible spectrum can be further divided into the blue (400-500 nm), green (500-600 nm), and red (600-700 nm) light that is the basis of all the colors we see (Chuvieco, 2009).

The infrared spectrum is significantly larger than the visible spectrum, ranging in wavelengths from about 700 to 14000 nm. The range is subdivided into the near infrared (700-1200 nm), the mid infrared (1200-8000 nm), and the thermal infrared (8000-14000 nm) regions (Chuvieco, 2009). The shortwave infrared is a range sometimes included as part of the mid infrared and is the region from approximately 1200 to 3000 nm (Chuvieco, 2009).

Hyperspectral vs. Multispectral

Imaging spectroscopy applies the principles of spectroscopy to every pixel in an image, combining the spatial presentation of an imaging sensor with the analytical capabilities of a spectrometer (Clark, 1999). The spectrometer measures the reflected electromagnetic radiation coming from the surface, dividing the incoming energy into bands of wavelengths. By obtaining electromagnetic spectra in a large number of spatial positions, a recognizable image of unique chemical bonds (and thus specific materials) can be created (Clark, 1999).

The information that can be conveyed by this image is dependent on the number and resolution of the bands. Each band is a slice of the electromagnetic spectrum and each contains different information about the materials being analyzed (Harris et al.). As is the case when approximating any curve, the smaller and more abundant the intervals (bands) are, the more accurately the spectrum can be drawn (Fig. 1). While multispectral images commonly contain less than ten bands that show discrete sections of wavelengths, hyperspectral images are comprised of hundreds of bands that create a continuum. The increased precision of hyperspectral data makes it possible to identify closely related materials and can show minute differences in spectra that may be smoothed over in multispectral data. The end product of the imaging spectrometer is an image with the addition of a third dimension in the form of spectral information (Pearlman, 2003).

STUDY AREA

The Turkana Basin is an East-African-Rift-System-related graben encompassing approximately 131,000 km^2 in northern Kenya and southern Ethiopia, which has been

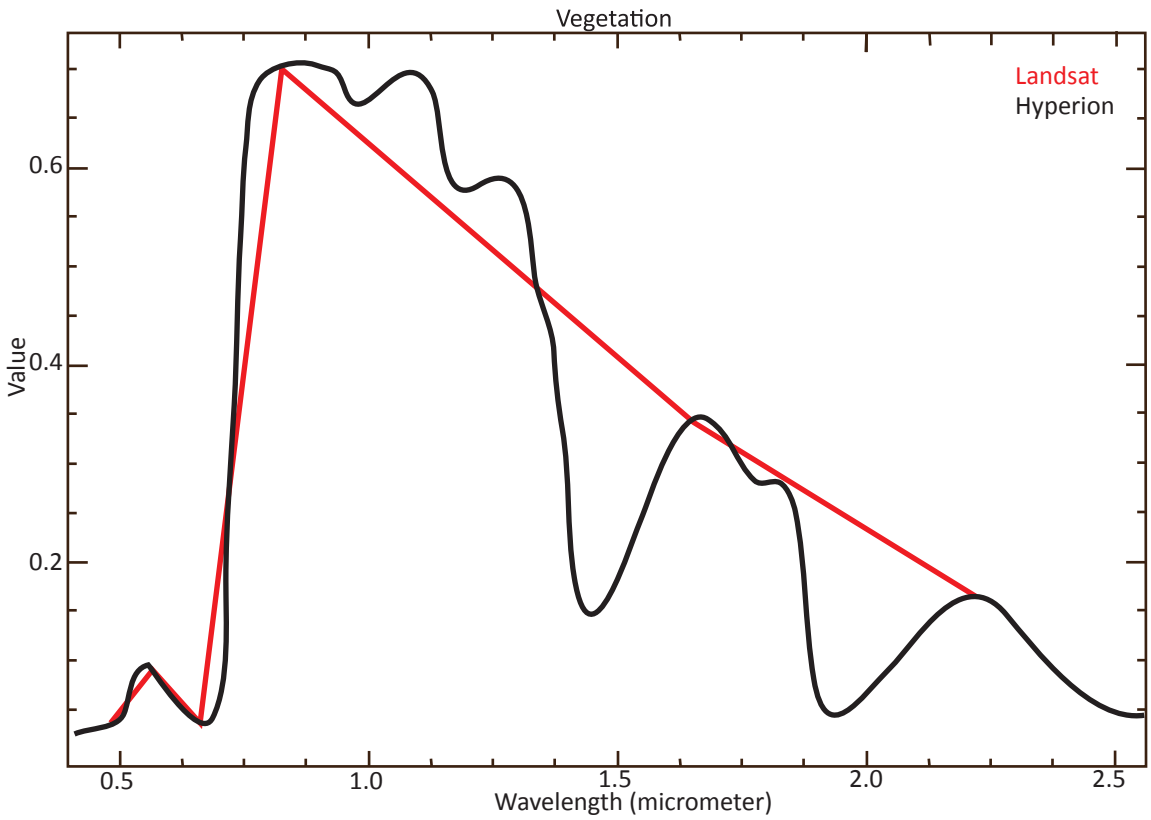

Figure 1. Comparison of a typical spectral signature for green vegetation as shown by the Landsat multispectral and Hyperion hyperspectral sensors. The spectrum made by Hyperion is formed with 242 continuous points, while the Landsat spectrum contains six discretely spaced points. Figure adapted from (EO-Miners, 2014).

intensively studied due to its abundant hominid and primate fossil record, (Haileab et al., 2004; Bruhn et al., 2011; Feibel, 2011). Contained in the basin is Lake Turkana, an alkaline lake primarily fed by the Omo River. Once connected to the Indian Ocean and the Nile River, faulting and lava emplacement have isolated the lake, though fossils and fluvial deposits still attest to the past connections (Bruhn et al., 2011; Feibel, 2011).

As in all rift settings, the East African Rift System hosts many alkaline suites of rocks. The Kenya Rift arm contains alkaline trachytic and phonolitic suites derived from various mafic parents as the result of fractional crystallization and crustal assimilation (Kabeto et al., 2001). The basement metamorphic rocks of the basin are part of the Mozambique Belt and formed during Precambrian mountain building events. It is overlain with sedimentary strata which are primarily quartzo-feldspathic sands derived from the quartzites, gneisses and schists of the Mozambique Belt and range in age from Cretaceous to Pleistocene (Feibel, 2011). Much of the basin is covered in thick volcanic tuffs and lava flows (Feibel, 2011).

The focus of this study is on an approximately 7.5 x 85 km area on the southeastern end of Lake Turkana (Fig. 2). The geology of the region of interest is dominated the Kulal basalt, a group that originated from Mt. Kulal to the east of Lake Turkana. K/Ar ages date the emplacement of the basalt to 3.01 ± 0.55 to 2.6 ± 0.02 Ma as well as 2.40 ± 0.03 to 2.04 ± 0.02 Ma (Bruhn et al., 2011).

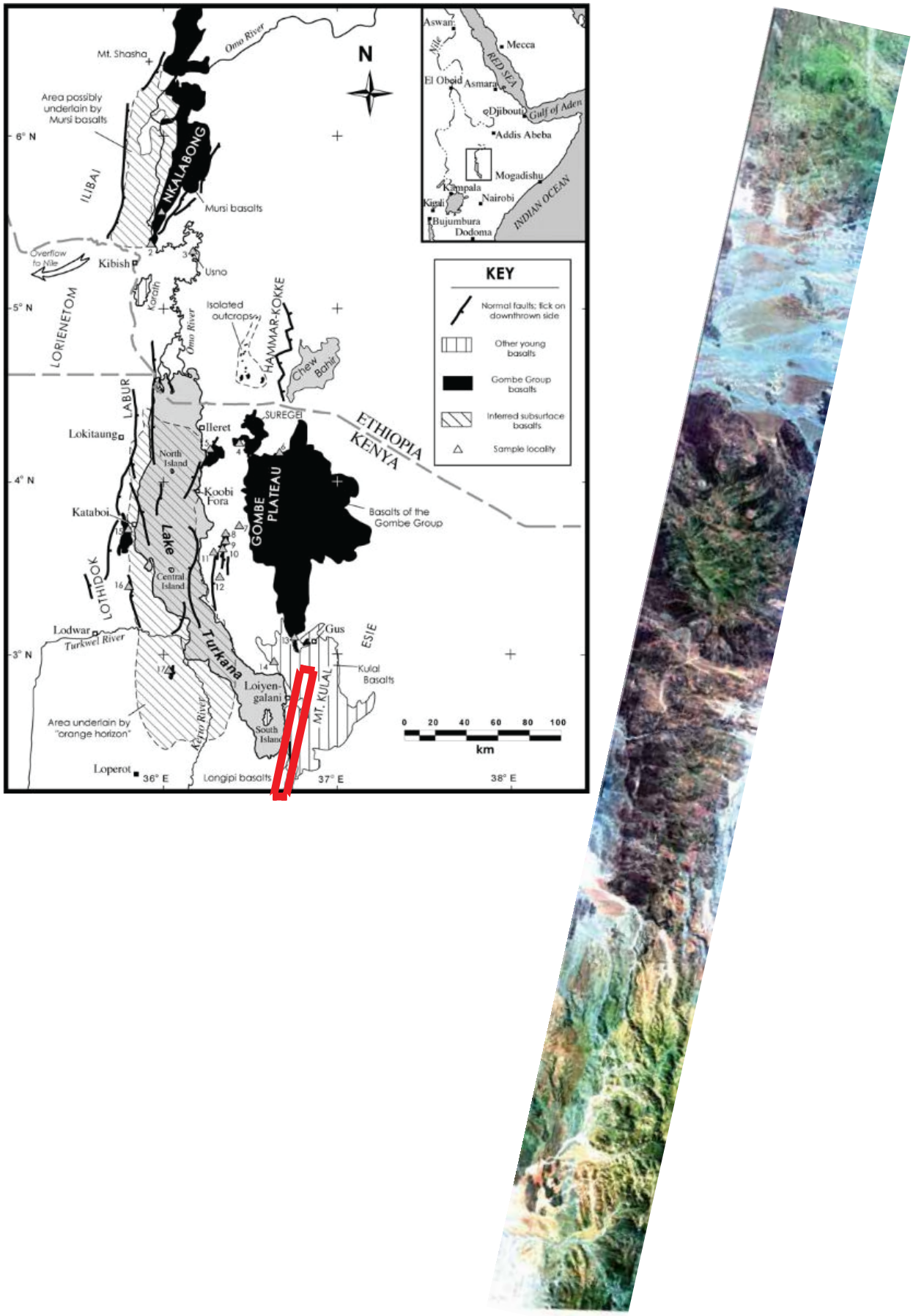

Figure 2. Location of study area relative to Lake Turkana, Kenya. A true color composite of the the original Hyperion imagery shows an aerial view. Bands 29,20,11 as R,G,B. Geologic map adapted from Haileab et al. (2004).

METHODS

The process of extracting spectral signatures to gain insight about the occurrence and distribution of surface geology is outlined in Figure 3 then laid out in more detail below.

Level 1R (L1R) radiometrically corrected Hyperion data and Level 1T (L1T) terrain corrected data were downloaded from the United States Geologic Survey's EarthExplorer website. Hyperion data commonly displays vertical stripes in the image that result from dark current imbalances and the pushbroom collection method of the sensor (Kruse, 2002). In order to remove the most obvious striping affects in the image, the acquired data were run through the Hyperion Tools toolkit developed by Devin White for ENVI users. Of the original 242 bands, many were uncalibrated and appeared blank, and others were deemed to be too noisy for further use. 154 L1R bands were selected for further analysis. Because the L1R data contains no spatial projection, the data had to first be geometrically corrected. This served the dual purpose of giving the image geographic coordinates as well as removing any spatial distortions. Corrections were done with the use of the L1T data and image-to-map registration of the two data sets. Using true color composite images, 20 ground control points were selected, and a RMS error of 0.789505 meters was achieved. By extracting the coordinates of the L1T GeoTIFF images at the selected control points and projecting the L1R data into WGS84 UTM Zone 37N, the L1R bands were geometrically corrected.

The final step in the preprocessing was atmospheric correction of the data. In order to make spectral analysis possible, the data were converted from radiance to reflectance. Because of complications due to edge effects and cloud cover, a spatial

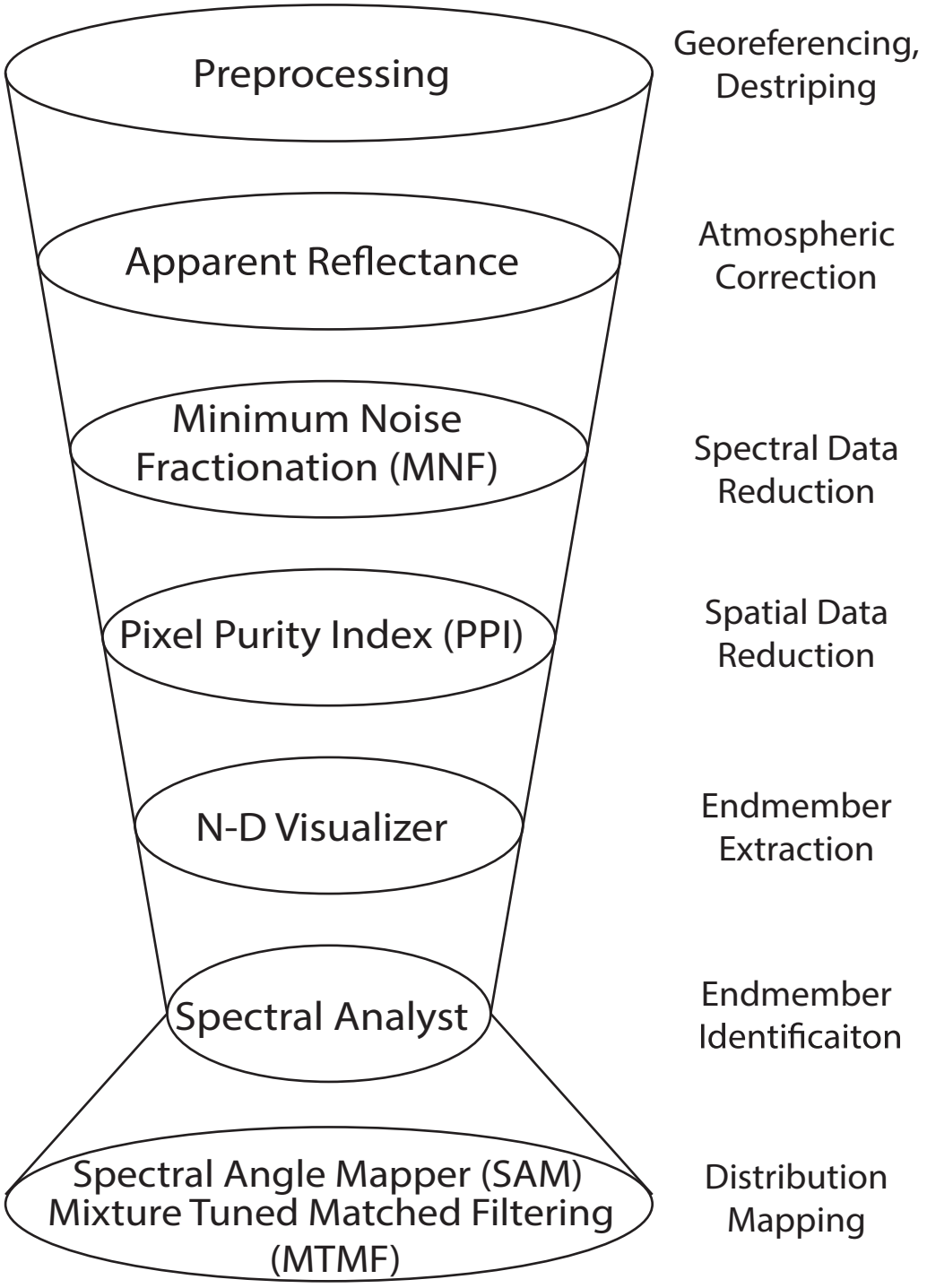

Figure 3. The workflow outlining the processing of hyperspectral data in ENVI. Input data begins as radiance before being spectrally and spatially subsetted, identified and reprojected as a distribution or abundance map. Figure adapted from ENVI (2006).

subset of the original data was taken to remove problem areas. This subset removed four pixels (120 meters) of each edge, and clipped out a region in the south with cloud cover. Atmospheric correction was done with the Flat Field Correction method, in which a spectrally flat and uniform area is selected, and its reflection values averaged. A bright area in the northwestern part of the image was selected to be the spectrally uniform baseline. The average reflectance value was subsequently divided into each pixel of the image in order to normalize the data and make it comparable to spectral library data. The conversion to reflectance should result in all pixels having a digital number value of 1.0 or less. This conversion produced an error on 379 (0.0167%) pixels, which have records exceeding the 1.0 value threshold.

Noise whitening and determination of data dimensionality using the Minimum Noise Fraction (MNF) transformation was the first step taken in the analysis of the image. The MNF function is essentially a series of two principal component analysis transformations that decorrelate the noise from the band information. Using a forward MNF rotation on the 154 input bands revealed the bands holding the most coherent information.

Eighteen MNF bands were selected as input of the Pixel Purity Index (PPI) function. The PPI finds the most spectrally pure (endmember) pixels in the image through repeated projection of n-dimensional scatter plots around a random unit vector. Pixels that project away from the majority of pixels represent those that have the least amount of mixing, and are the potential endmembers. These pixels are saved and a tally of the number of times each is marked as extreme is kept. The more times a pixel is marked as spectrally pure, the more likely it is comprised of a single material. Once

these possible endmembers were identified, they were subsetted to remove all pixels that were found within four pixels of the edge. Further subsetting removed all pixels that displayed reflectance values exceeding 1.0 in any band.

The results of the PPI analysis were brought into ENVI's n-D visualizer function for manual visual inspection and interpretation. Using the 18 MNF bands selected in previous steps gave the data cloud a dimensionality of 18 for which to rotate the scatter plot of data points around. The goal of this analysis was to identify which of the potentially pure pixels are similar to one another, and which are the most likely to contain only one type of material. These pixels are those that separate themselves from the group when projected in scatter plots. Those that are spectrally similar will form a group, and the groups of unique spectra represent the endmembers that are the basis of data interpretation.

Those endmembers deemed to be unique classes of pure pixels were compared to a series of spectral libraries. These libraries contain the spectra of hundreds of materials which are used to identify the classes extracted from the n-D visualizer. Many spectral libraries come standard with the ENVI 5.0 software, 10 of which were used in this study. All library spectra were collected with a Beckman spectrophotometer by the United States Geological Survey (USGS). Mineral and vegetation spectra were provided by the USGS mineral, USGS dry vegetation and USGS green vegetation libraries. Results were also compared to whole rock libraries which were provided by Johns Hopkins University. Spectra for coarse- and fine-grained igneous, metamorphic, and sedimentary rocks were divided into six separate libraries. The final library was of soil spectra, again provided by Johns Hopkins University. The endmembers were compared against the spectral libraries

using the automatically generated validity score as well as discretion based on visual appearance and knowledge of the study area.

The production of maps was the final step in the analysis process. Two mapping methods were used. The first was the spectral angle mapper (SAM) method, an automated method for comparing image to library spectra that makes use of the spectral angles between the two spectra. The user selects the input spectra against which each image pixel is compared to, then both the observed (pixel) and reference (library) spectra are projected onto vectors in n-dimensional space, where n is the number of bands. By setting a threshold (measured in radians) for the angle of separation between the pixel's vectors, each pixel is determined to either match or not match the input spectra (Fig. 4). In this way, the method is concerned with the shape of the spectra being compared. SAM is considered a whole pixel analysis technique because it produces maps of the dominant spectra of each pixel, essentially determining if a pixel contains the materials of interest (ENVI, 2006).

The second mapping technique is a sub pixel analysis technique that attempts to estimate the sub-pixel abundances of each endmember, acting under the assumption that the reflectance spectrum of each pixel is a linear combination of the identified endmembers. The Mixture Tuned Matched Filtering (MTMF) mapping method uses spectral linear unmixing and the user-defined endmembers to display sub-pixel abundances of each material. Using rule and infeasibility images adds a manual interpretation aspect to the analysis to minimize the high false positive rates that accompany other linear unmixing methods (ENVI, 2006). By plotting rule vs. infeasibility scores on a 2-D scatter plot, the user can select to display

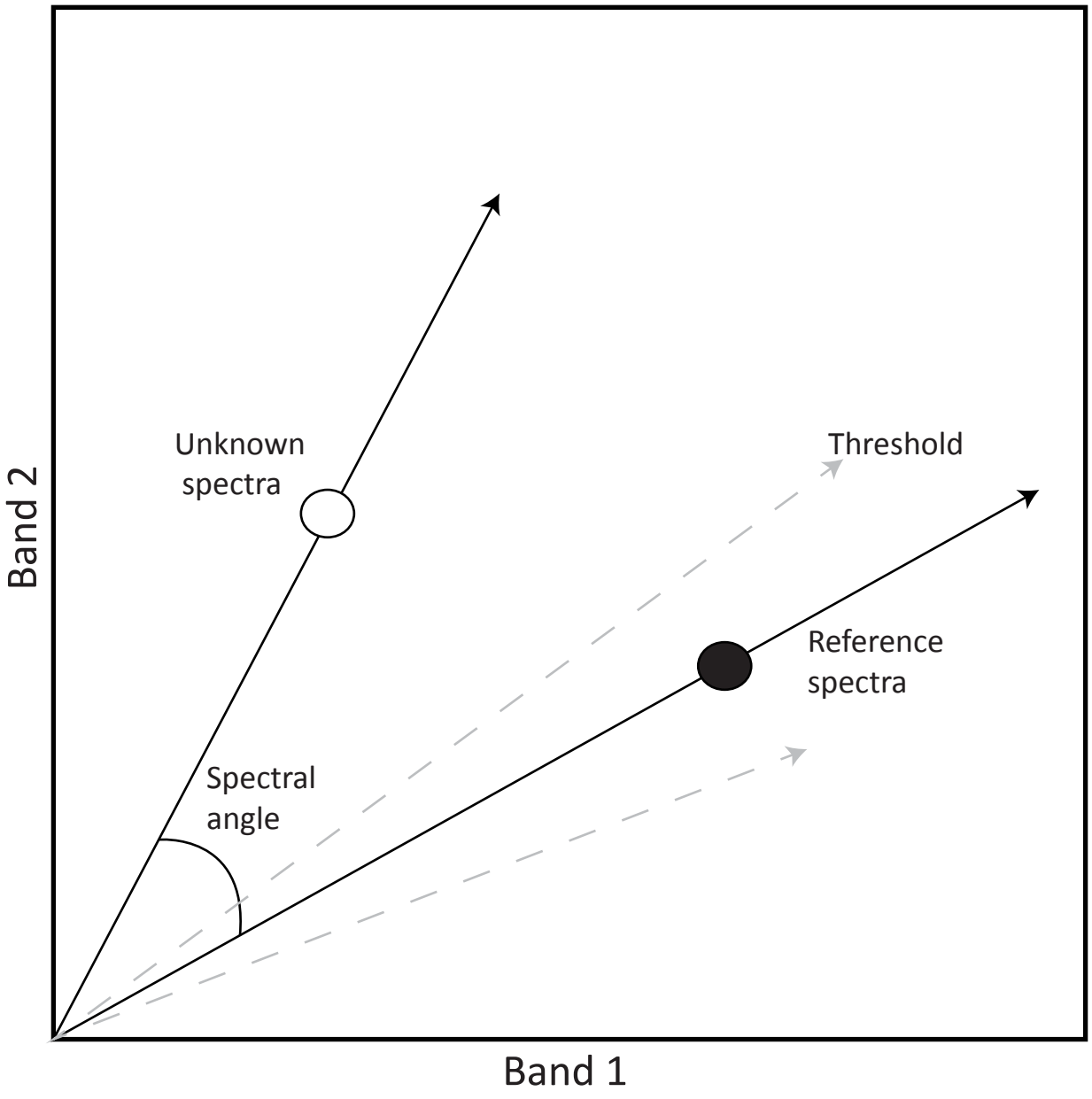

Figure 4. A simplified, two dimensional diagram of the Spectral Angle Mapper (SAM) method of pixel classification. The unknown spectra are contained in an image pixel. If the unknown spectra falls within the user-defined spectral angle threshold, a positive match is recorded. Figure modified from (ENVI, 2006).

only the pixels with the highest rule and lowest infeasibility scores in order to find those that best fit the endmember spectra (ENVI, 2006).

RESULTS

Figure 5 displays the mean spectra of the identified endmembers on the same plot as the best spectral library match. The classes that best matched the library spectra were selected to be mapped with both the SAM and MTMF mapping techniques as displayed in Figures 6 and 7 respectively. Accompanying both map results are the rule images. Each endmember that is mapped is given a rule image that provides a way of visually interpreting whether the mapped distribution of the endmember is valid. Further analysis with the SAM method was done using library selected endmembers instead of the user-selected ones. Inputs of basalt and gneiss did not yield viable results, though the presence of hematite was confirmed.

DISCUSSION

No spectra resembled that of n-D class 12 (Fig. 5k) though analysis with satellite imagery revealed its location to be in the waters of Lake Turkana. Based on the automatic generation of a best fit score and manual visual interpretation, goethite, hematite, coast sage, kaolinite/smectite, desert varnish 1, and lamprophyre (Fig. 5b, d, f, g, h, and j) were deemed to be good matches against the library spectra. With the exception of coast sage, further interpretation of the image was based on the above spectra.

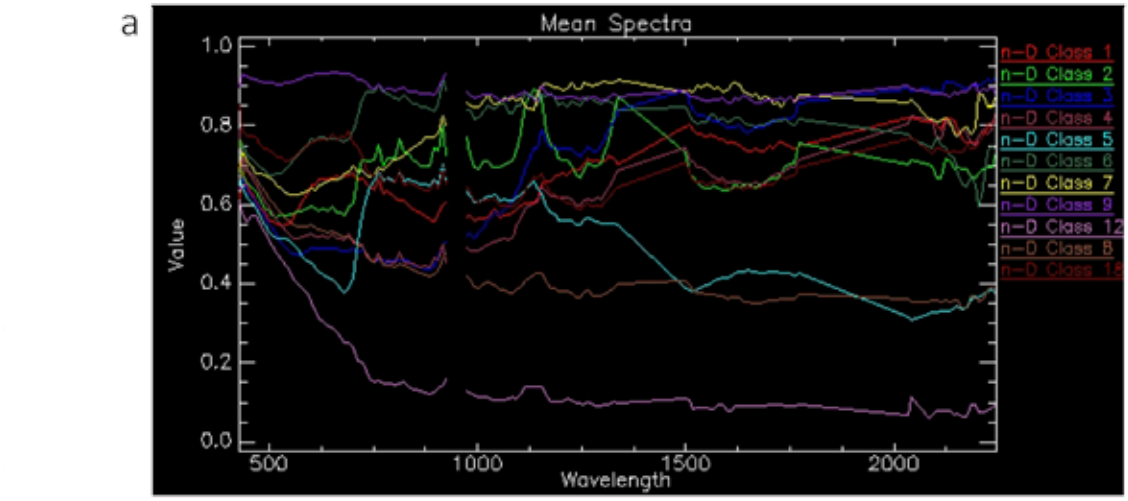

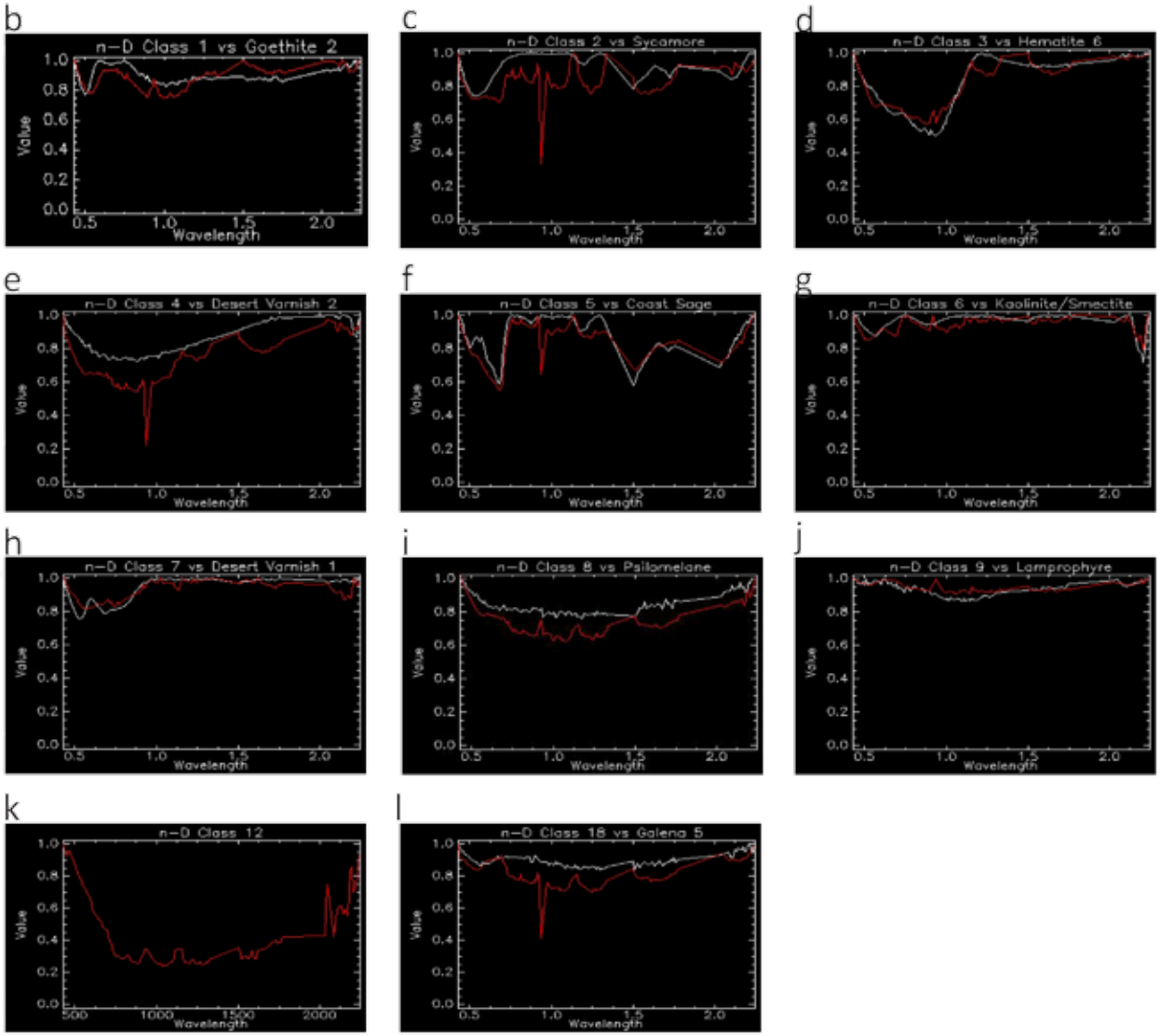

Figure 5. a) Mean spectra of selected endmembers as manually determined by regions of interest in the n-D visualizer. Wavelength in nm. b-l) Spectra of selected endmembers in red compared to their closest match shown in white. No library spectra resembled k. Wavelength in µm. Spectra show a pronounced peak or dip from 922.54 - 972.99 nm in the comparison spectra. This range is absent in the mean spectra and should be ignored.

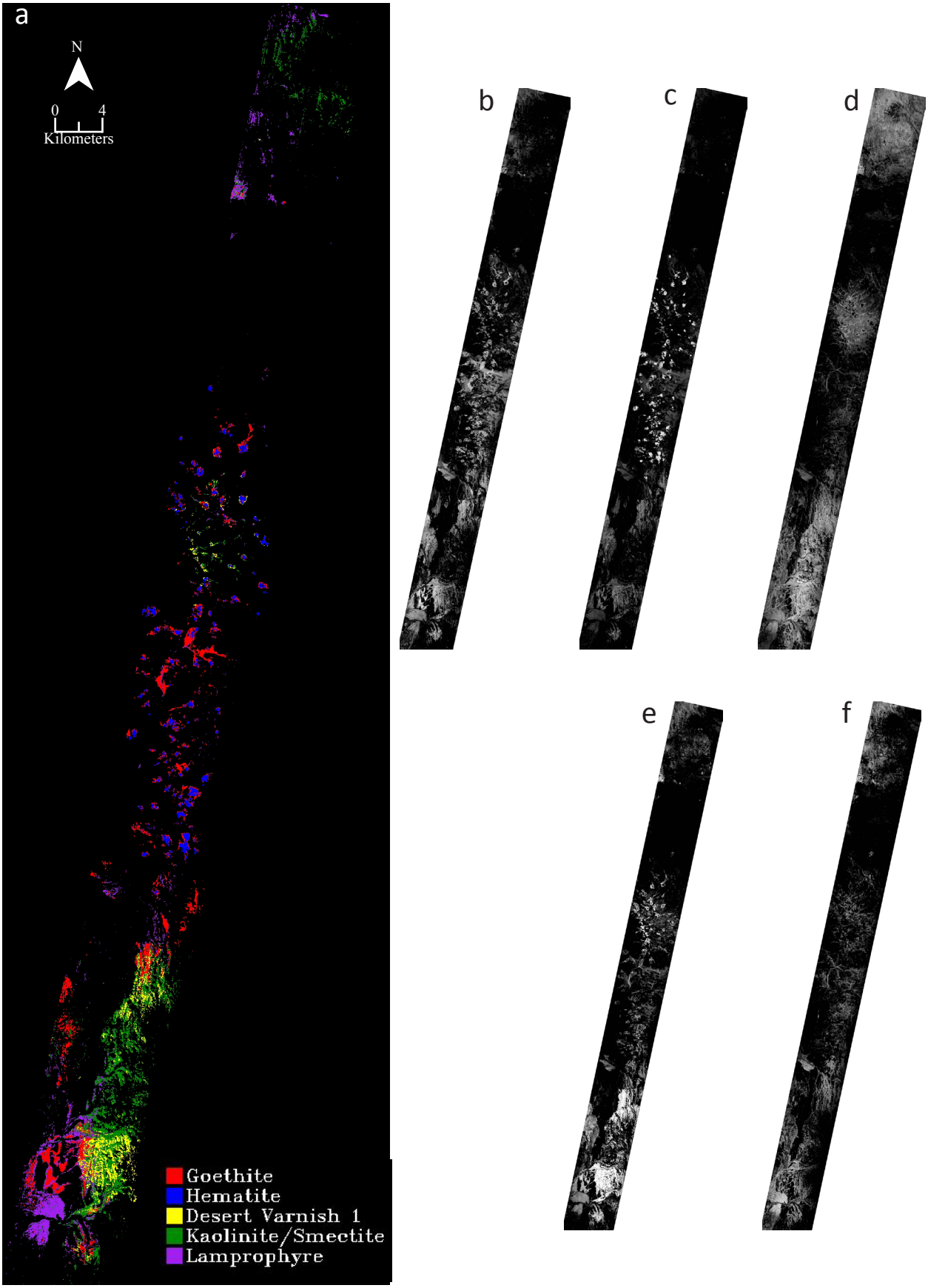

Figure 6. Spectral Angle Mapper (SAM) results (a) and the rule images for goethite (b), hematite (c), desert varnish 1 (d), kaolinite and smectite (e) and lamprophyre (f). Brighter pixels in rule images indicate a higher probability of the pixel containing the respective endmember.

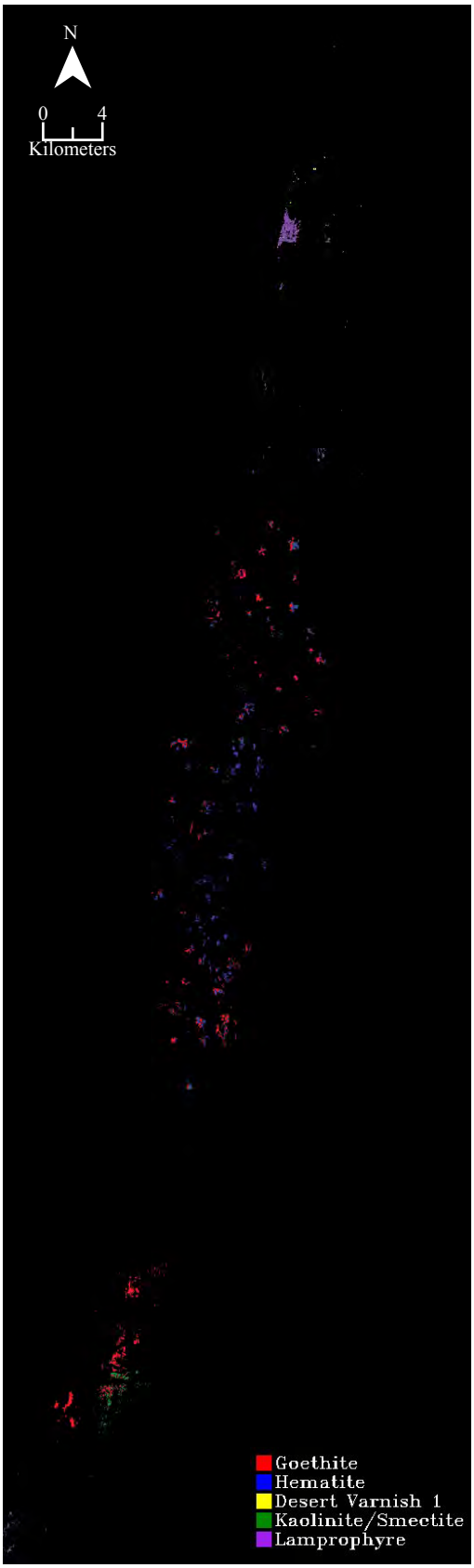

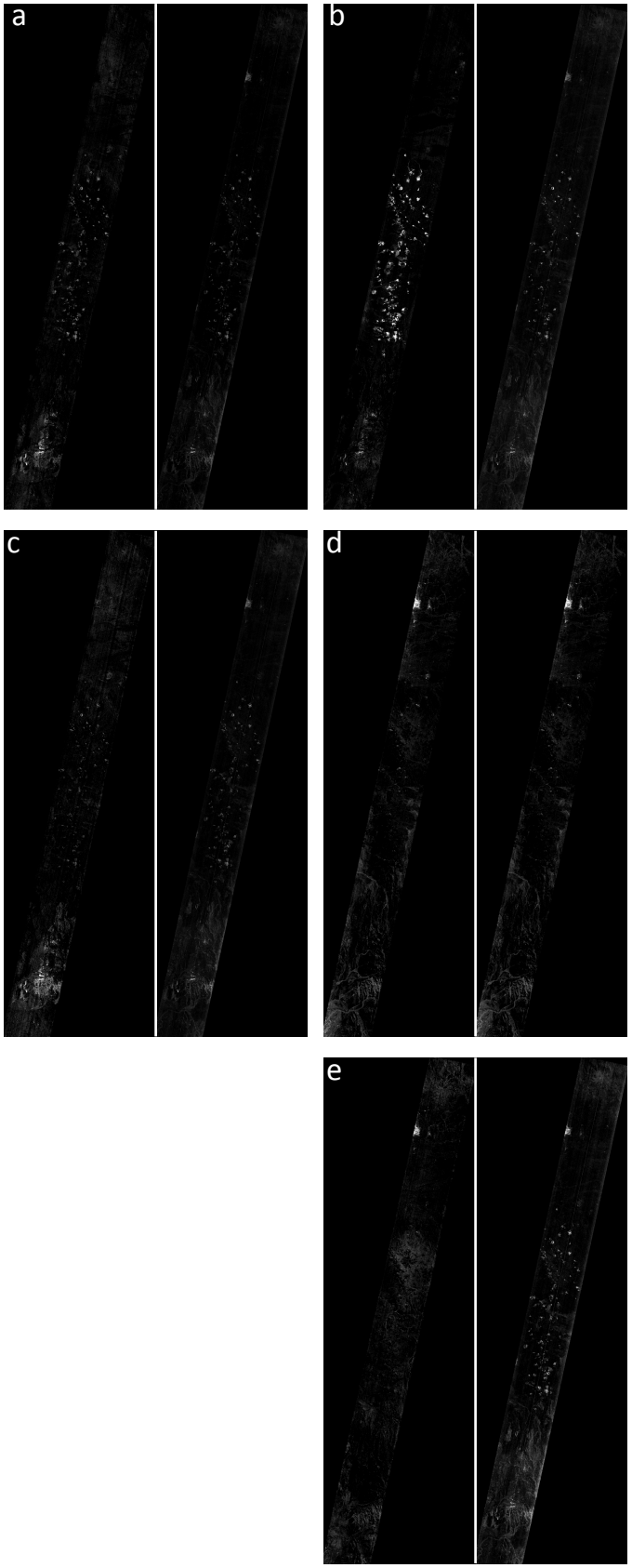

Figure 7. Composite images of Mixture Tuned Matched Filtering (MTMF) maps of goethite (a), hematite (b) kaolinite and smectite (c), desert varnish 1 (d) and lamprophyre (e). Score images for each material are on the left and display pixels that likely contain that material with bright pixels. Infeasibility images are on the right, and show pixels with high probability of false positives in with bright pixels. Pixels with a good match for the material should have a high score and a low infeasibility value.

Spectral Angle Mapper (SAM)

When compared to a true color image (Fig. 2) the endmember groups distributed throughout the SAM map show a distinct spatial correlation to visible landforms. Immediately apparent are the areas of goethite and hematite primarily concentrated in the center of Figure 6. More specifically, they align with the bright red peaks visible in the basalt. On the bottom of the image is a region in which the spectra of desert varnish, kaolinite/smectite and lamprophyre dominate the SAM map. Both kaolinite/smectite and lamprophyre exist to a less prominent extent in the northern part of the image. The rule images associated for each mineral validate the results, as the brightest values in the rule images are strongly correlated with the distribution shown in the SAM image. Pixels colored black in the SAM image remained unclassified either as a result of being unidentified as an endmember, or being identified as an endmember that was not selected to be a part of the map. For example, the northern region of the image is the most heavily vegetated and the spectrum for coast sage dominates, however the pixels that would be classified as coast sage are left out of the interpretation and thus are black.

Mixture Tuned Matched Filtering (MTFM)

The purpose of the MTMF analysis was to provide another interpretation method to compare with the distribution mapped with the SAM technique. Taking advantage of the ability of the MTMF technique to extract strong matches from possible false positives, the MTMF image was used as a way to validate the SAM results. Figure 8 offers a side-by-side comparison which clearly shows that there are significantly fewer

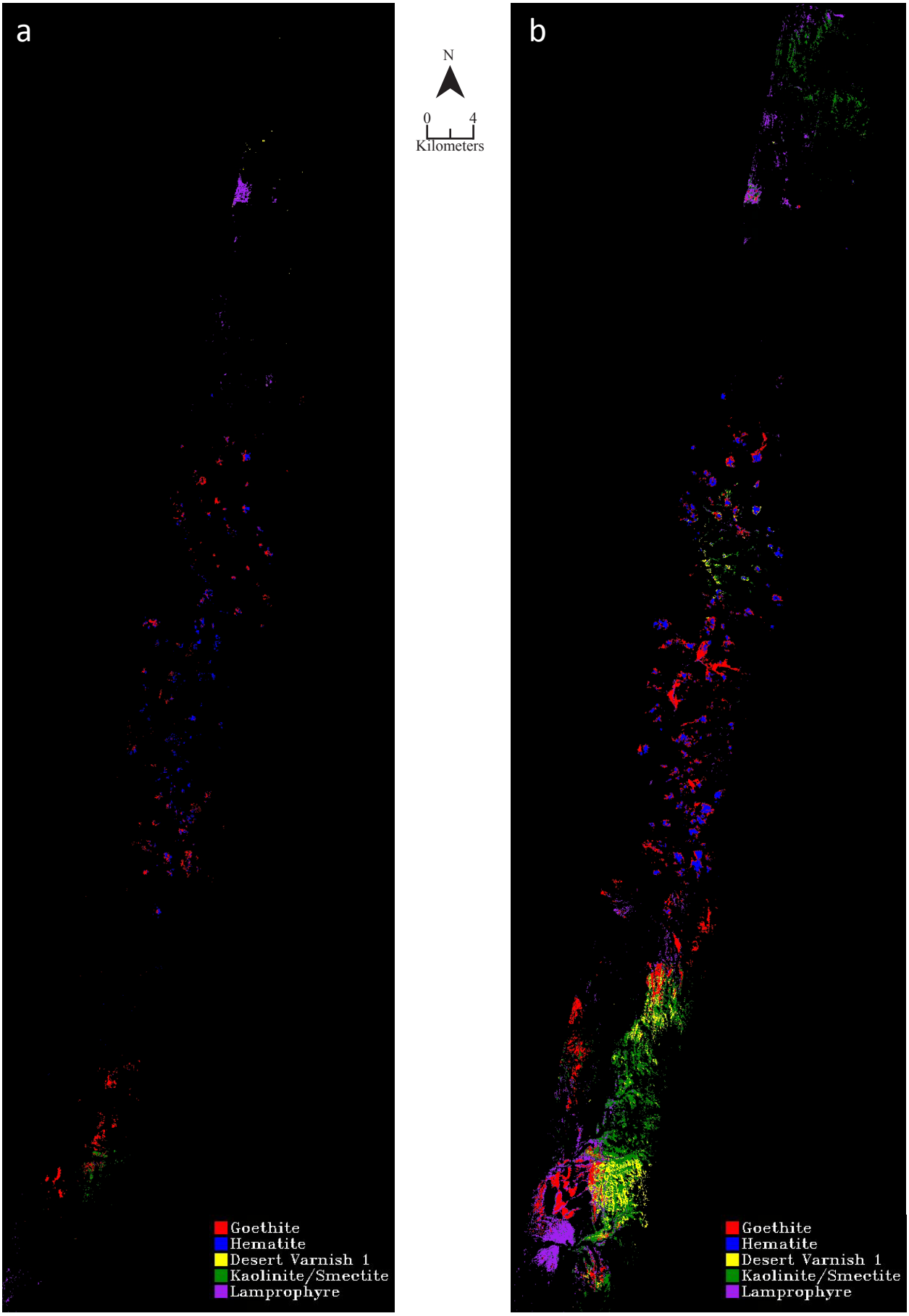

Figure 8. Comparison of a) Mixture Tuned Matched Filtering (MTMF) and b) Spectral Angle Mapper (SAM) results.

pixels in the MTMF image. This can be attributed to conservative selection of pixels on the part of the user as well as exclusion of pixels that were false positives in the SAM image. Most notable is the greatly reduced extent of desert varnish, kaolinite/smectite and lamprophyre in the southern part of the image. In the center of both maps, both hematite and goethite are present, speaking to the ability of the SAM technique to correctly identify both minerals. The northern portion of the MTMF image is generally absent of the abundant lamprophyre and kaolinite/smectite seen in the SAM with the exception of one area of lamprophyre. Taken together, the combination of SAM and MTMF results definitively point to the presence of all five endmembers, though hematite and goethite show the highest correlation between both maps.

Mineral Endmembers

The interpretation of both spectral and map results is not complete without knowledge of the identified endmembers. It is important to note that the results from the spectrometer show only what is happening at the very surface. Goethite, hematite, smectite, kaolinite and desert varnish are all common weathering products associated with the basaltic and gneissic parent rocks in the study area. With this is mind, the results of the mapping appear logical.

Goethite (FeO(OH)) and hematite (Fe_2O_3) are iron oxides that are often associated with the weathering of basalt. In a spectroscopic study of weathered basalt, Wang et al. (1999) found hematite to be the dominant mineral on the weathered surface of the rock, both in terms of spectra and abundance. Minerals themselves often give rise to other minerals when weathered. When olivine, a major component of basalt, is

weathered in oxidizing conditions, a combination of smectite and goethite called iddingsite is formed. When weathering of the olivine crystal nears completion, goethite is the dominant product (Smith et al., 1987). When forming soil from basaltic parent material, both hematite and goethite are common. The formation of goethite at the expense of hematite is favored by lower temperatures, higher water activity, lower levels of Fe release from the basalt, higher organic matter and lower pH level (Smith et al., 1987). Both hematite and goethite are direct products of the oxidation of basalt, and form a red coating over the rock. It is this iron rich layer, not the basalt, that is registered by the spectrometer. The peaks seen in Figure 9 are found in the center of the study area and exhibit the distinct red color indicative of the weathering process. When compared to the SAM and MTMF map results, there is no doubt that it is these peaks that register as hematite and goethite.

Kaolinite ($Al_2Si_2O_5(OH)_4$) is a clay mineral and smectite is a family of clays. Both are common weathering products of felsic minerals, but can also form as the result of the weathering of mafic rock such as basalt (Righi et al., 1999). Kaolinite has been shown to form in conjunction with halloysite in gneissic weathering profiles. More generally, potassium feldspar weathers to form kaolinite in weathering profiles, hydrothermal alteration zones, and sedimentary rocks (Ruiz Cruz; Papoulis et al., 2004). Kaolinite and smectite have been shown by Righi et al. (1999) to form in soils derived from basalt. Their study concluded that kaolinite forms within layers of smectite crystals, and that this combination dominates the clay fraction of the soil. These clay minerals make sense in the geologic context of the area as the weathering products of both basalt and the basement gneisses and other metamorphic rocks. Their spectra registers in areas that appear absent of basalt and are instead dominated by sediment.

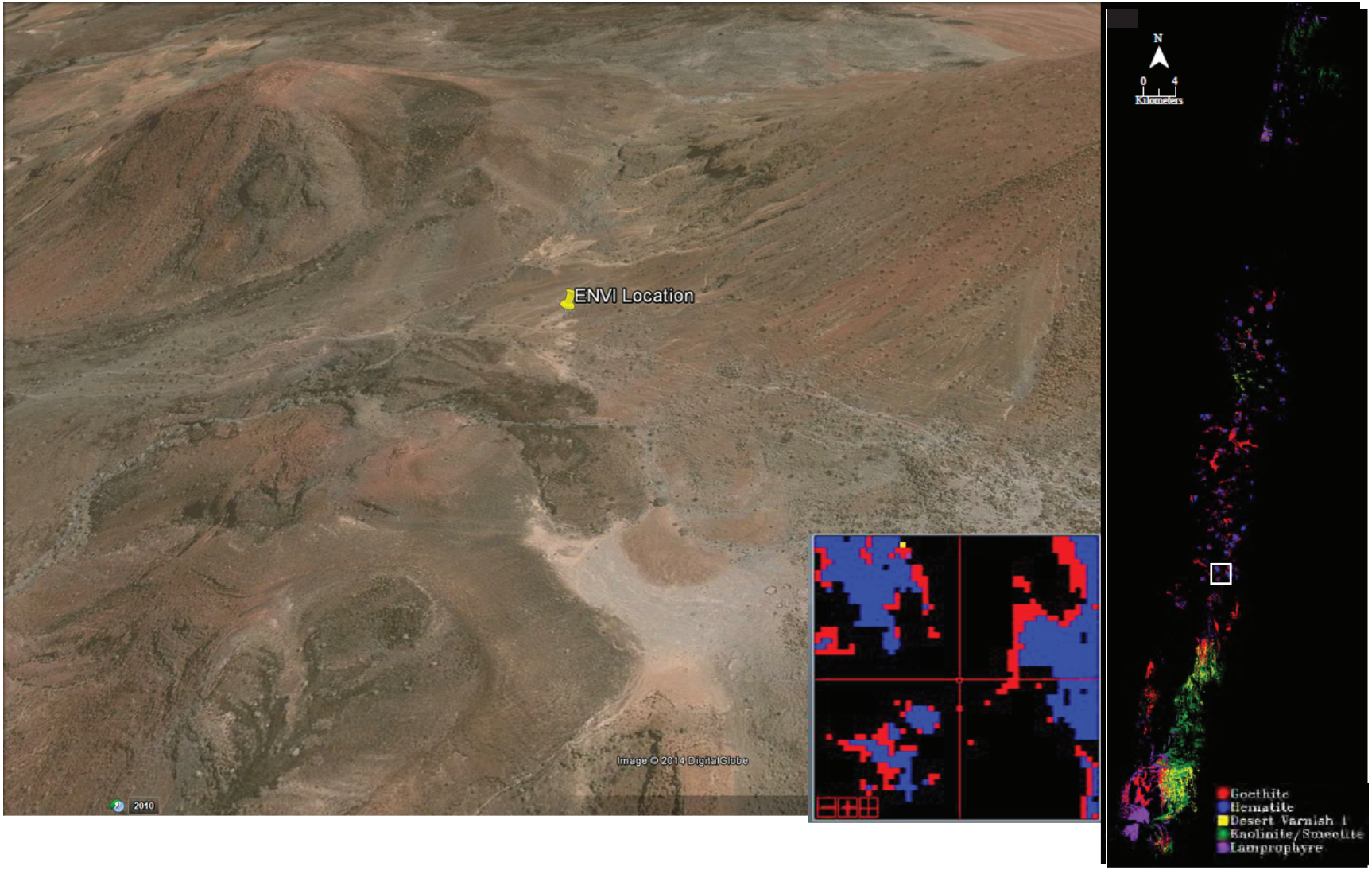

Figure 9. Google Earth image of three typical examples of the red peaks that dominate the center of the distribution maps. Image has been tilted to emphasize the relief of the peaks. Accompanying the image is the SAM map for the same area. The crosshairs in the zoom image align with the pushpin in the satellite image. Blue pixels in the zoom indicate hematite while red correspond to goethite.

Based on spectral library results, the spectra of these clay-rich areas were best described as kaolinite/smectite, a mixture shown by Righi et al. (1999) to be common in soils.

Third, desert varnish is a general term for the thin (~20 microns) layer that forms on rock surfaces in arid environments. The layer is created when clays, often with Fe, Mn and Mg metals, are transported by wind to the surface of rocks and stick to form a resilient coating. The varnish can be found on any rock so long as the conditions are right. Though the clay particles and metals are results of weathering, the varnish is formed from external sources, and is not connected to the rock on which the varnish sits (Allen, 1978). Desert varnish is a very common occurrence in arid areas such as the Turkana basin where a lack of precipitation allows the layer to form and become permanent. Being a mixture of the minerals listed above, it is no surprise that it exists in the study area.

The final endmember of interest on the map is lamprophyre, the only whole-rock endmember. Lamprophyre is a rock that cannot as easily be confirmed in the study area, but remains a strong possibility. Interested in the composition of the Gombe group basalts found to the north of this study's study area (Fig. 2), Haileab et al. (2004) collected samples in the vicinity of the study area for the purposes of geochemical analysis. Their findings indicate only the presence of basalt, with total alkali content ($K_2O + Na_2O$) not reaching levels high enough to be classified as lamprophyre. However, these findings do not exclude the possibility of lamprophyre existing in the area. As mentioned before, rift systems produce alkali rich rocks, and their existence in the Kenya Rift segment of the East African Rift System has been well documented (Kabeto et al., 2001). Though often stated as being an uncommon rock group, Rock

(1987) argues that lamprophyre is not as rare as generally assumed and can be found in a diverse range of tectonic settings. The most common in rift settings such as the Turkana Basin are rich in alkali (Moayyed et al., 2008). The proximity of the study area to known emplacements of alkaline rock coupled with the demonstrated ability of Hyperion data to provide quality interpretations merits consideration of the existence of lamprophyre in the study area.

Investigating with SAM

Recall from previous sections that the primary function of the SAM mapping method is to identify whether a material is present. Input endmember spectra can be selected from those extracted from pixels as was done in previous steps, or directly from any input contained in a spectral library. When this is done, the user is essentially asking the question: "Is this material present in the image?" In order to search for the rocks known to exist in the region, the spectra of basalt and gneiss were mapped with the SAM technique, as they are known to exist in the area. Johns Hopkins University spectral library provides 12 different spectra for basalt. Inputting each spectrum of the fine and coarse grained igneous samples surprisingly failed to provide even a single pixel match, until the threshold angle was set to 0.5 radians, five times that of the largest threshold of the user extracted endmember SAM inputs. Even then, only one class was found and it was located in the waters of Lake Turkana.

A similar result was obtained when the 11 spectra of gneiss from the fine and coarse grained metamorphic libraries were matched against the image pixels. Two classes were found at an angle threshold of 0.5 radians, with one located in the water of

the lake. The other was located in the south of the image. To test the validity of the methods, the spectra of hematite, the best fit of the user selected endmembers, was selected. Three classes of hematite were mapped, at a threshold angle of 0.1 radians. The distribution of these hematite endmembers was closely aligned with the locations of hematite in the SAM image in Figure 6, attesting to a failure the combination of Hyperion data and available spectral libraries to locate spectra of basalt and gneiss, and not a flaw in the methodological process.

CONCLUSIONS

Air- and spaceborne hyper- and multispectral sensors have played an instrumental role in efforts to map regional-scale areas for the purposes of geologic mapping and remote mineral exploration. One such instrument is the EO-1 Hyperion spaceborne hyperspectral spectrometer, launched in November of 2000 (Kruse, 2002). Hyperion has demonstrated an ability to accurately identify minerals in areas of hydrothermal alteration (Crosta et al., 2008; Nikolakopoulos et al., 2008; Diaz-Castellon et al., 2012; Ball et al., 2013). Analysis of Hyperion data through SAM and MTMF maps and rule images of showed the presence of goethite, hematite, and kaolinite/smectite, desert varnish and lamprophyre to exist at the southern end of Lake Turkana, Kenya.

The results of the map display only what is on the very surface of the Earth. As common products of weathering, the desert varnish and goethite, hematite, kaolinite, and smectite minerals cover the weathered and oxidized basalt that covers the area. These products essentially create a mask over the rocks on which they formed, dominating the spectral signature read by the spectrometer. Therefore it is no surprise that these minerals

are seen in abundance in the image. The identification of lamprophyre in the image was less expected. Previous studies in the area identified only the existence of basalt, and reported nothing about lamprophyre (Haileab et al., 2004). This raises the exciting possibility that a previously unidentified region of alkaline rock lies within the study area. If true, it provides a testament to the ability of remote sensing techniques to accurately classify large areas. While it is easy for the geologist to generalize the extent of an area or misclassify a rock, a spaceborne spectrometer can provide insight about details as small as chemical composition.

The five spectra that did not match with spectral library data were likely mainly caused by the impurity of the pixels. Measures are taken by both the user and the program to include only the purest endmembers, though it would be surprising to actually find an example of a totally pure 30 x 30 meter square in the real world. As there will inevitably be more than a single material in the pixel, those that were not matched with a spectral library profile likely represent pixels with too much spectral mixing to be recognized as a single material. A finer spatial resolution would solve this problem, as it increases the likelihood of finding only a single material within a pixel. Another problem may lie in outside influences. Looking at the true color composite in Figure 2, there appears to be water in the region near the top of the image. Also note that this area is absent of classification in both the SAM and MTMF output maps. The water will obscure any material that it covers and may alter the spectra of the materials around it by changing the reflectance values.

Taken as a whole, the images created through the analysis of EO-1 Hyperion data indicate the instrument is a viable means of acquiring information about regional-sized

study areas. In fact, the use of hyperspectral imaging spectroscopy may have revealed a previously misinterpreted or undiscovered area of lamprophyre in a dominantly basaltic region. In order for the existence of this lamprophyre (as well as the goethite, hematite, smectite/kaolinite, and desert varnish) to be verified, further interpretation with ground truthing and physical samples are required.

ACKNOWLEDGEMENTS

First and foremost I would like to thank Tsegaye Nega who provided inspiration for the project and whose guidance and knowledge was instrumental in its execution. I would also like to extend thanks to Bereket Haileab, whose expertise in Turkana Basin geology provided a link to that which I could only see on a screen. I am also grateful for the technical support given by Wei-Hsin Fu and the Carleton College GIS lab. Finally, thanks are due to all faculty and students in the Carleton College Geology Department whose support was of tremendous assistance.

REFERENCES CITED

Allen, C. C., 1978, Desert varnish of the Sonoran Desert; optical and electron probe microanalysis: Journal of Geology, v. 86, p. 743-752.

Ball, J. L., Calder, E. S., Hubbard, B. E., and Bernstein, M. L., 2013, An assessment of hydrothermal alteration in the Santiaguito lava dome complex, Guatemala: implications for dome collapse hazards: Bulletin of Volcanology, v. 75.

Bruhn, R. L., Brown, F. H., Gathogo, P. N., and Haileab, B., 2011, Pliocene volcano-tectonics and paleogeography of the Turkana Basin, Kenya and Ethiopia: Journal of African Earth Sciences, v. 59, p. 295-312.

Chuvieco, E. a. A., H., 2009, Fundamentals of Satellite Remote Sensing: Boca Raton, FL, CRC Press, 436 p.

Clark, R. N., 1999, Spectroscopy of Rocks and Minerals, and Principles of Spectroscopy, Manual of Remote Sensing: Remote Sensing for the Earth Sciences: New York, John Wiley and Sons, Inc, p. 3-58.

Crosta, A., Cardoso, D. B., and Anonymous, 2008, Mapping supergene and hydrothermal alteration minerals using EO-1/hyperion in the El Salvador porphyry-Cu deposit, Chile: International Geological Congress, Abstracts = Congres Geologique International, Resumes, v. 33, p. 0-Abstract 1341573.

Curtiss, B., Shiley, D. A., and Anonymous, 2012, Rapid mineralogical analysis in support of mineral exploration and mine development: International Geological Congress, Abstracts = Congres Geologique International, Resumes, v. 34, p. 2124.

Diaz-Castellon, R., Hubbard, B. E., Carrasco-Nunez, G., and Rodriguez-Vargas, J. L., 2012, The origins of Late Quaternary debris avalanche and debris flow deposits from Cofre de Perote volcano, Mexico: Geosphere, v. 8, p. 950-971.

ENVI, 2006, Spectral Analysis With ENVI, ENVI Training Series: Boulder, CO, ITT Visual Information Systems, 123 p.

EO-Miners, 2014, Earth Observation in the frame of EO-MINERS - Overview of remote sensing methods, sensors and applications: (last accessed 3/11/2014)

Feibel, C. S., 2011, A Geological History of the Turkana Basin: Evolutionary Anthropology, v. 20, p. 206-216.

Guerschman, J. P., Hill, M. J., Renzullo, L. J., Barrett, D. J., Marks, A. S., and Botha, E. J., 2009, Estimating fractional cover of photosynthetic vegetation, non-photosynthetic vegetation and bare soil in the Australian tropical savanna region upscaling the EO-1 Hyperion and MODIS sensors: Remote Sensing of Environment, v. 113, p. 928-945.

Haileab, B., Brown, F. H., McDougall, I., and Gathogo, P. N., 2004, Gombe group basalts and initiation of Pliocene deposition in the Turkana depression, northern Kenya and southern Ethiopia: Geological Magazine, v. 141, p. 41-53.

Jacobson, S., Khan, S., and Anonymous, 2006, Identifying surface alterations caused by hydrocarbon microseepages in the Patrick Draw area of southwest Wyoming, using image spectroscopy and hyperspectral remote sensing: Abstracts: Annual Meeting - American Association of Petroleum Geologists, v. 15, p. 52.

Kabeto, K., Sawada, Y., and Wakatsuki, T., 2001, Different evolution trends in alkaline evolved lavas from the northern Kenya Rift: Journal of African Earth Sciences, v. 32, p. 419-433.

Khan, S., Shah, M. T., Biber, K., and Anonymous, 2011, Towards the better understanding of gold mineralization in the northern areas of Pakistan: Abstracts with Programs - Geological Society of America, v. 43, p. 513.

Kruse, F. A., 2002, Comparison of AVIRIS and Hyperion for Hyperspectral Mineral Mapping, 11th JPL Airborne Geoscience Workshop: Pasadena, CA.

Lu, P., Wang, L., Niu, Z., Li, L., and Zhang, W., 2013, Prediction of soil properties using laboratory VIS-NIR spectroscopy and Hyperion imagery: Journal of Geochemical Exploration, v. 132, p. 26-33.

Mauger, A. J., Keeling, J. L., and Huntington, J. F., 2007, Alteration mapping of the Tarcoola Goldfield (South Australia) using a suite of hyperspectral methods: Transactions - Institution of Mining and Metallurgy. Section B: Applied Earth Science, v. 116, p. 2-12.

Moayyed, M., Moazzen, M., Calagari, A. A., Jahangiri, A., and Modjarrad, M., 2008, Geochemistry and petrogenesis of lamprophyric dykes and the associated rocks from Eslamy peninsula, NW Iran: Implications for deep-mantle metasomatism: Chemie der Erde - Geochemistry, v. 68, p. 141-154.

Nikolakopoulos, K., Tsombos, P., and Anonymous, 2008, Comparison of multispectral (EO-1 ALI, Landsat ETM), and hyperspectral (EO-1 Hyperion) remote sensing data for geological mapping: International Geological Congress, Abstracts = Congres Geologique International, Resumes, v. 33, p. 0-Abstract 1324505.

Onuma, T., Yajima, T., Hayashi, T., Yamamoto, K., and Anonymous, 2005, Alteration zoning extracted by spaceborne hyperspectral data analysis: Shigen Chishitsu, v. 55, p. 11-24.

Papoulis, D., Tsolis-Katagas, P., and Katagas, C., 2004, Progressive stages in the formation of kaolin minerals of different morphologies in the weathering of plagioclase: Clays and Clay Minerals, v. 52, p. 275-286.

Pearlman, J. S. B., P.S.; Segal, C.C.; Shepanski, J.; Beiso, D.; Carman, S.L., 2003, Hyperion, a space-based imaging spectrometer IEEE Transactions on Geoscience and Remote Sensing v. 41, p. 1160-1173.

Petrovic, A., Khan, S. D., and Chafetz, H. S., 2008, Remote detection and geochemical studies for finding hydrocarbon-induced alterations in Lisbon Valley, Utah: Marine and Petroleum Geology, v. 25, p. 696-705.

Pignatti, S., Cavalli, R. M., Cuomo, V., Fusilli, L., Pascucci, S., Poscolieri, M., and Santini, F., 2009, Evaluating Hyperion capability for land cover mapping in a fragmented ecosystem: Pollino National Park, Italy: Remote Sensing of Environment, v. 113, p. 622-634.

Pour, A. B., Hashim, M., and van Genderen, J., 2013, Detection of hydrothermal alteration zones in a tropical region using satellite remote sensing data: Bau goldfield, Sarawak, Malaysia: Ore Geology Reviews, v. 54, p. 181-196.

Riaza, A., Buzzi, J., Garcia-Melendez, E., Vazquez, I., Bellido, E., Carrere, V., and Muller, A., 2012, Pyrite mine waste and water mapping using Hymap and Hyperion hyperspectral data: Environmental Earth Sciences, v. 66, p. 1957-1971.

Righi, D., Terribile, F., and Petit, S., 1999, Pedogenic formation of kaolinite-smectite mixed layers in a soil toposequence developed from basaltic parent material in Sardinia (Italy): Clays and Clay Minerals, v. 47, p. 505-514.

Rock, N. M. S., 1987, The nature and origin of lamprophyres: an overview: Geological Society, London, Special Publications, v. 30, p. 191-226.

Ruiz Cruz, M. D., Genesis and evolution of the kaolin-group minerals during the diagenesis and the beginning of metamorphism, p. 12.

Smith, K. L., Milnes, A. R., and Eggleton, R. A., 1987, Weathering of basalt; formation of iddingsite: Clays and Clay Minerals, v. 35, p. 418-428.

van der Meer, F. D., van der Werff, H. M. A., van Ruitenbeek, F. J. A., Hecker, C. A., Bakker, W. H., Noomen, M. F., van der Meijde, M., Carranza, E. J. M., Smeth, J. B. d., and Woldai, T., 2012, Multi- and hyperspectral geologic remote sensing: A review: International Journal of Applied Earth Observation and Geoinformation, v. 14, p. 112-128.

Wang, A., Jolliff, B. L., and Haskin, L. A., 1999, Raman spectroscopic characterization of a highly weathered basalt; igneous mineralogy, alteration products, and a microorganism: Journal of Geophysical Research, v. 104, p. 27-27,077.